International Journal of Heat and Fluid Flow 61 (2016) 68–74

Contents lists available at ScienceDirect

International Journal of Heat and Fluid Flow

journal homepage: www.elsevier.com/locate/ijhff

Experimental and numerical investigation of a strongly-forced precessing cylinder flow

Thomas Albrecht[a,*], Hugh M. Blackburn[a], Patrice Meunier[b], Richard Manasseh[c], Juan M. Lopez[d]

[a] Department of Mechanical and Aerospace Engineering, Monash University, VIC 3800, Australia
[b] IRPHE, CNRS, and Aix–Marseille Université, 49 Rue Joliot-Curie, 13013 Marseille, France
[c] Department of Mechanical and Product Design Engineering, Swinburne University of Technology, VIC 3122, Australia
[d] School of Mathematical and Statistical Sciences, Arizona State University, Tempe, AZ 85287, USA

ARTICLE INFO

Article history:
Available online 28 June 2016

Keywords:
Precession
Inertial waves
Instability
Symmetry breaking
Triadic resonance
PIV
DNS

ABSTRACT

Planar particle image velocimetry (PIV) and direct numerical simulations (DNS) of the flow in a precessing cylinder of height-to-radius ratio of 1.835 are presented for a nutation angle of 15° and a Reynolds number 6430 based on the cylinder's angular frequency. We find excellent agreement in terms of time-averaged velocity profiles and Kelvin mode amplitudes during the initial development and in the asymptotic state. In the experiment, a rapid transition to a disordered state follows a brief appearance of azimuthal structures with a predominant wavenumber $m = 9$. In the DNS, the transition occurs later than in the experiment, and shows dominance of a triad of azimuthal wavenumbers $m = 1, 4, 5$ during the transient evolution. Adding a small random perturbation to the simulation after the forced mode is established accelerates transition to flow dominated by $m = 9$ which eventually transitions to a disordered state, consistent with observations from PIV. The breaking of rotoreflection (inversion) symmetry of the system is found to be critical in establishing evolution paths to the disordered and asymmetric asymptotic state.

1. Introduction and background

Rotating flows are present in the atmosphere, in oceans and lakes, in astrophysical and many technical applications. A rotating system allows for inertial waves to exist owing to the restoring effect of the Coriolis force. One way to excite inertial waves is precession, the simultaneous rotation around two axes as sketched in Fig. 1: a cylinder of radius R and height H, tilted through an angle α and rotating at an angular frequency Ω_1, is mounted on a turntable which rotates at Ω_2. Precession is considered as a possible driver for the geo-dynamo, i.e. the creation of Earth's magnetic field (Malkus, 1968; Giesecke et al., 2015, and references therein). Also, liquid fuel in spin-stabilised spacecraft may be subject to precessional forcing, destabilising the whole spacecraft (Manasseh, 1993).

Some types of instability and transition of rotating flows may be associated with Kelvin modes, the linear, inviscid eigenmodes of solid-body rotation flow. Although not solutions of the full Navier–Stokes equations with no-slip boundary conditions, at sufficiently large Reynolds number they can be useful diagnostics of experimental and numerical observations in contained flows. In addition, they have served as the basis of a theoretical model for a triadic resonance instability mechanism which has been shown to work well in modelling behaviour in the weakly nonlinear regime within a cylinder, near onset of instability in the presence of weak precessional forcing (Albrecht et al., 2015; Meunier et al., 2008). In the present work we have used planar projections onto low-order Kelvin modes as one basis for comparison of large-scale energetics from experiment and DNS, though their utility is limited in attempting to completely describe flows in the strongly forced (and ultimately disordered) regime, which is the focus of our attention. We note, however, that triadic resonance mechanisms may still exist even when Kelvin mode descriptions are inadequate; the minimum requirement is that azimuthal wavenumbers and temporal frequencies of participating structures satisfy the triad conditions (see Section 2.3 Albrecht et al., 2015). For example, in a precessing cylinder, the directly forced flow has fundamental azimuthal

* Corresponding author. Tel.: +61435015543.
E-mail addresses: thomas.albrecht@monash.edu (T. Albrecht), hugh.blackburn@monash.edu (H.M. Blackburn), meunier@irphe.univ-mrs.fr (P. Meunier), rmanasseh@swin.edu.au (R. Manasseh), jmlopez@asu.edu (J.M. Lopez).

http://dx.doi.org/10.1016/j.ijheatfluidflow.2016.05.009
0142-727X/

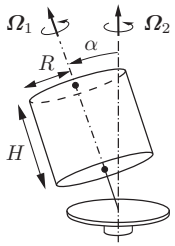

Fig. 1. Schematic of precessional forcing: a cylinder of radius R and height H, rotating at $\boldsymbol{\Omega_1}$, is tilted through a nutation angle α and is mounted on a turntable which rotates at $\boldsymbol{\Omega_2}$.

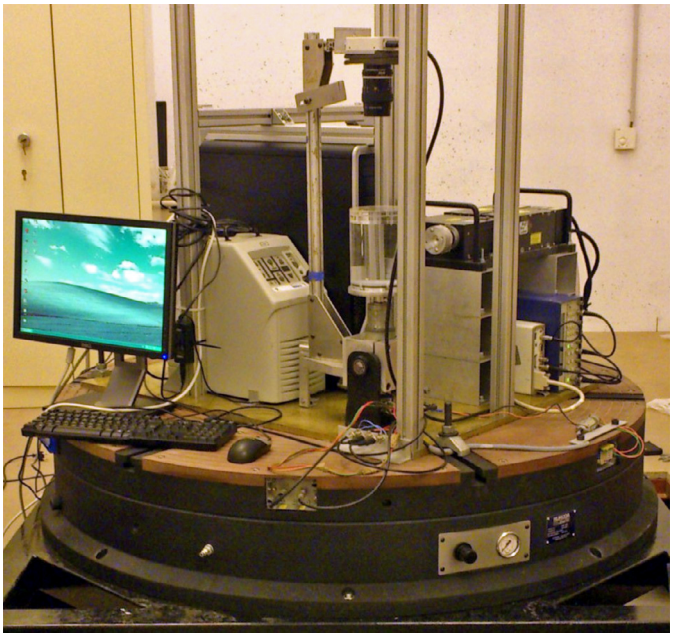

Fig. 2. Experimental setup: water-filled cylinder, PIV camera, laser and computer, all mounted on a rotating table.

wavenumber $m = 1$, so that the azimuthal wavenumbers of other structures participating in a triad instability with this component must sum to unity.

2. Experimental set-up and PIV procedure

Fig. 2 shows the experimental set-up. A cylinder, filled with water and spinning at $\boldsymbol{\Omega_1}$, is mounted on a DC motor's axis. A rotary encoder measures the motor's angular velocity with an accuracy of 0.1%. The cylinder is made from Perspex and has an inner radius $R = 46.2\text{mm} \pm 0.1\text{mm}$. Its effective height H can be varied by using different inserts. Aligned with the axis and facing the cylinder's top, a Redlake ES 11000 11-megapixel camera records PIV images. Motor, cylinder and camera are mounted on a gimbal which can be tilted to an angle α of up to 15° using a linear stepper motor. The accuracy of the tilt angle is 0.1°. A light sheet created by a 250 mJ dual-pulse NdYAG laser (Big Sky Laser) and cylindrical lenses illuminates a cross-section of the tilted cylinder at a height z_{PIV}. The coordinate system is fixed at the centre of the cylinder. Together with a PC controlling the camera, all of the above is mounted on a large platform rotating at $\boldsymbol{\Omega_2}$.

The total angular velocity along the axis of the cylinder in the inertial frame of reference is

$$\Omega = \Omega_1 + \Omega_2 \cos\alpha. \tag{1}$$

Initially, the cylinder was spinning upright (i.e. with $\alpha = 0$) to establish a solid-body rotation. It was then tilted (defining $t = 0$)

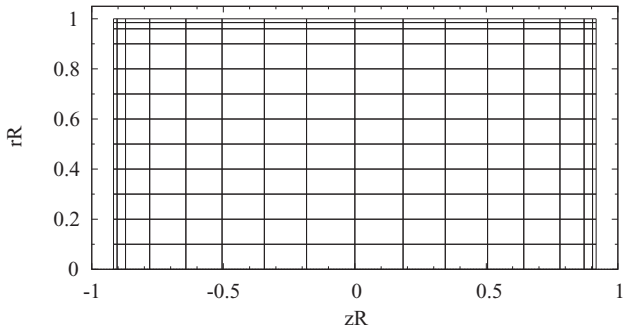

Fig. 3. Spectral element mesh of the meridional semi-plane for a cylinder of height:radius ratio $\Gamma = 1.835$.

and 200 image pairs (the maximum permitted by available memory) of the transient flow were recorded at 1Hz. An image pair had a time separation of $\Delta t = 11\,\text{ms}$, during which the cylinder turned approximately 2°. The PIV resolution was 0.0419 mm/px. Grid refinement (final window size 64×64 px), a 50% image overlap, and image shifting were applied. The seeding particles (Optimage Ltd) had a nominal diameter of 30 μm and a density of $1 \pm 0.02\,\text{kg/m}^3$.

Since the camera is mounted in the gimbal frame of reference, it mainly records solid-body rotation flow. To extract the secondary flow, we subtract the cylinder rotation by counter-rotating the image pairs prior computing the PIV cross-correlation. For this, it is essential to know the exact centre of rotation in image coordinates since errors in its position, $\Delta\boldsymbol{x}_c$, introduce a spurious mean velocity $\sim \Delta\boldsymbol{x}_c/\Delta t$. We found that the centre of rotation in image coordinates could differ between experiments (when the cylinder was removed and replaced) or even move during one experiment (during the tilting, although the cause of the centre shift remains unclear). We therefore adopted a mostly automatic procedure to obtain the centre of rotation for each experiment individually, consisting of: (*i*) iteratively identifying the cylinder wall at eight azimuthal locations by finding radial step changes of image brightness averaged over segments of 15°, (*ii*) fitting an ellipse to the eight wall locations, and (*iii*) time-averaging the centre to eliminate wobbling due to a slight misalignment of cylinder axis and its rotation axis.

3. Computational method

The computational methodology is similar to that employed in Albrecht et al. (2015), with a cylindrical coordinates spectral element–Fourier method for the incompressible Navier–Stokes equations (Blackburn and Sherwin, 2004), solved in a reference frame which after tilt-over rotates steadily with angular velocity $\boldsymbol{\Omega_2}$. The system was non-dimensionalised using the cylinder radius R as the length scale, and the cylinder rotation rate $1/\Omega_1$ as the time scale. The cylindrical coordinates are $\boldsymbol{r} = (r, \varphi, z)$ and the corresponding velocity is $\boldsymbol{u} = (u, v, w)$. The non-dimensional governing equations are

$$\frac{\partial \boldsymbol{u}}{\partial t} + \boldsymbol{u}\cdot\nabla\boldsymbol{u} + \frac{2}{\Omega_1}\boldsymbol{\Omega_2}\times\boldsymbol{u} + \frac{1}{\Omega_1}\frac{\mathrm{d}\boldsymbol{\Omega_2}}{\mathrm{d}t}\times\boldsymbol{r} = -\nabla p + \frac{1}{Re}\nabla^2\boldsymbol{u},$$
$$\text{with} \quad \nabla\cdot\boldsymbol{u} = 0, \tag{2}$$

where any terms that can be written as gradients of a scalar are absorbed into the pressure gradient term, and p is the reduced pressure. The results presented below were computed in the gimbal frame of reference, in which the boundary conditions on all cylinder walls are $u = w = 0$ and $v = r$, and the initial condition is solid-body rotation, $(u, v, w) = (0, r, 0)$.

The spectral element mesh used had 192 spectral elements covering the meridional semi-plane, as shown in Fig. 3, and 128 data planes (64 Fourier modes) in azimuth. Local mesh refinement is

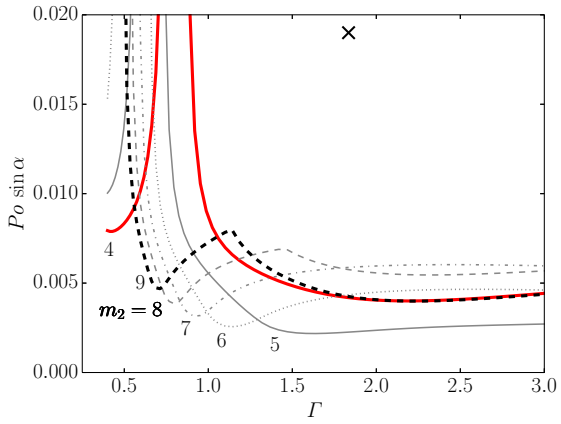

Fig. 4. Critical forcing amplitude ($Po\sin\alpha$) at which triadic resonance occurs between the forced (1, 1, 1)-Kelvin mode and two free Kelvin modes of azimuthal wave number m_1 and $m_2 = m_1 + 1$, as predicted by weakly nonlinear theory (Lagrange et al., 2011). This theory includes viscous effects, and the outcomes here are for $Re = 6430$. The cross corresponds to the parameters for the present investigation.

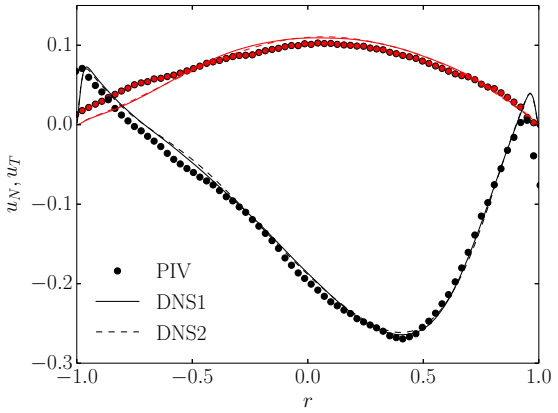

Fig. 5. Time-averaged, non-dimensional velocity components normal (u_N, black) and tangential (u_T, red) to the tilt direction, extracted along a diameter normal to the tilt direction, obtained from PIV (symbols) and DNS (lines) in the asymptotic state with $\Gamma = 1.835$, $Po \approx -0.0689$, $\alpha = 15^\circ$ and $Re = 6430$, taken at $z = z_{\mathrm{PIV}} = 0.25\Gamma$. Data from two DNS runs with different perturbation histories are almost indistinguishable.

concentrated near the walls to resolve the boundary-layer structure. Sixth-order tensor-product nodal basis functions are used in each element, giving at total of 7081 independent mesh nodes for each data plane and 906,368 nodes in total. We have checked this resolution is adequate to resolve flows for the parameters employed.

In the present work, we focus on the case $\Gamma = H/R = 1.835$, $\alpha = 15^\circ$, $Po = \Omega_2/\Omega_1 = -0.0689$, $Re = 6430$ and compare experimental results to DNS at identical parameters. The Reynolds number is similar to that employed in Lagrange et al. (2008) and Blackburn et al. (2014) and well above the theoretical instability threshold for triadic resonances (Lagrange et al., 2011) of $Re = 1167$ at the given angle, yet small enough for the flow to be computed with moderate computational resources. With the parameters employed, the (1, 1, 1)-Kelvin mode is forced at its first resonance. The three integers (n, l, m) are the number of axial half wavelengths, the lth root of the dispersion relation, and the azimuthal wavenumber, respectively. Further details are given in Albrecht et al. (2015). Note that this aspect ratio does not result in an *exact* resonant triad, as was studied in Lagrange et al. (2008). Here, no two parasitic modes exist that are exactly resonant with the forced mode. Fig. 4 is a plot of the curves at which various triadic resonances occur between the forced (1, 1, 1)-Kelvin mode and two free Kelvin modes with azimuthal wavenumbers m_1 and $m_2 = m_1 + 1$ in $(\Gamma, Po\sin\alpha)$-space for fixed $Re = 6430$, as predicted by weakly nonlinear theory (Lagrange et al., 2011). The cross symbol in the figure is the location in this parameter space at which the results presented here were obtained, showing that it is well beyond the onset of the primary triadic resonances.

4. Validation and post-processing

Fig. 5 compares time-averaged data obtained from PIV (symbols) and DNS (lines) in the asymptotic state to assess the accuracy of both approaches. Velocity components normal and tangential to the plane of tilt, u_N and u_T, were extracted along a diameter at $z = z_{\mathrm{PIV}} = 0.25\Gamma$. There is very good agreement between the experimental and DNS data over most of that domain, with minor deviations near the cylinder wall, giving confidence in the fidelity of both the experimental measurements and the simulations.

Radial and azimuthal velocity components, u and v, from the PIV plane were projected onto an equivalent slice of the Kelvin mode's velocity components u_j and v_j, as described in Meunier et al. (2008). We assume that the in-plane velocity at height z consists of a sum of Kelvin modes, each rotated by angle β_j, is given by

$$\begin{bmatrix} u \\ v \end{bmatrix} = Ro \sum_j a_j \sin(k_j z) \begin{bmatrix} -\mathrm{i}\sin(\varphi + \beta_j) u_j(r) \\ \cos(\varphi + \beta_j) v_j(r) \end{bmatrix} + \text{c.c.}, \tag{3}$$

where $Ro = (\Omega_2/\Omega)\sin\alpha$, and c.c. denotes complex conjugation. Exploiting the orthogonality of the Kelvin modes, one can obtain the non-dimensional amplitudes a_j.

A useful diagnostic measure for the DNS data is the kinetic energy per unit volume contained in azimuthal Fourier mode m

$$E_m = \frac{1}{2A} \int_A \widehat{\boldsymbol{u}}_m \cdot \widehat{\boldsymbol{u}}_m^* \, r \, \mathrm{d}A, \tag{4}$$

where $A = \Gamma R^2$ is the area of the meridional semi-plane, and $\widehat{\boldsymbol{u}}_m$ is azimuthal mode m of the Fourier transform of the velocity field in the cylinder frame of reference.

The governing equations and the boundary conditions are equivariant under a rotoreflection (inversion) symmetry, $\mathcal{I}$. The action of this inversion symmetry on the position vector is $\mathcal{I}\boldsymbol{r} = -\boldsymbol{r}$, its action on the cylindrical coordinates is $(r, \varphi, z) \mapsto (r, \varphi + \pi, -z)$, and its action on the velocity is

$$\mathcal{A}(\mathcal{I})(u, v, w)(r, \varphi, z, t) = (u, v, -w)(r, \varphi + \pi, -z, t). \tag{5}$$

A parameter that quantifies the symmetry of a flow is

$$S = ||\boldsymbol{u} - \mathcal{I}\boldsymbol{u}||_2, \tag{6}$$

where $S \geq 0$, and $S = 0$ means that the velocity field under consideration is inversion symmetric; see Marques and Lopez (2015) for details.

5. Initial dynamics and transition to disordered flow

To replicate the experiment, we ran two simulations at the same parameter values, corresponding to the experimental conditions, but with slightly different transient schedules. For one case, DNS1, the flow is initially in solid-body rotation with $\alpha = 0$, and at $t = 0$ the cylinder is tilted over to $\alpha = 15^\circ$ smoothly in a time corresponding to 1/10 of a cylinder rotation period; no other disturbances were modelled. In the experiment, a linear stepper motor tilts the cylinder over a similar period, but no attempt was made to smooth the stepper motor's ramp-up and ramp-down. The other simulation, DNS2, is initiated in the same way as DNS1, but at

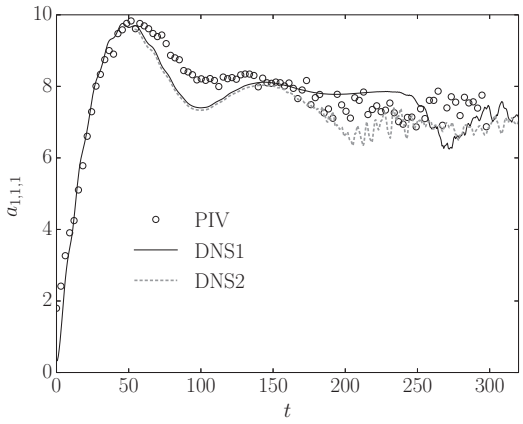

Fig. 6. Amplitude of the (1, 1, 1)-Kelvin mode, $a_1 = a_{1,1,1}$, extracted from PIV (symbols), DNS1 (solid line), and DNS2 (dotted line).

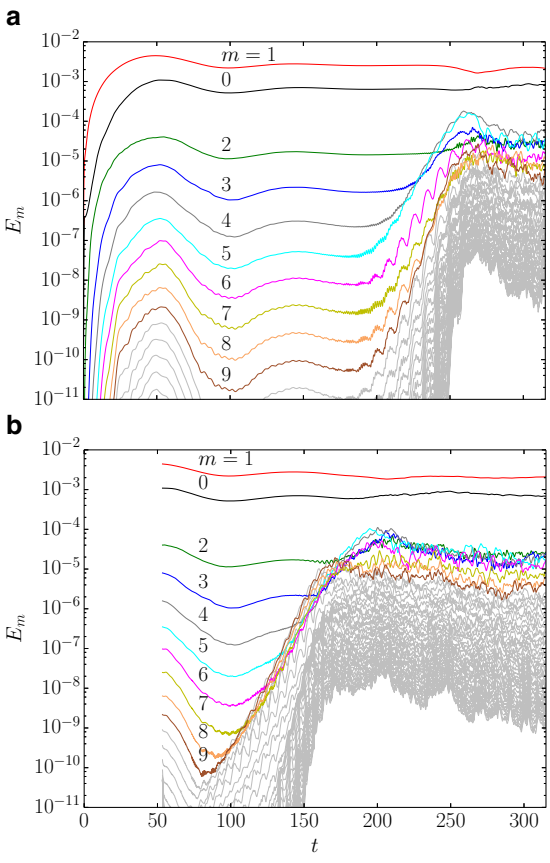

Fig. 7. Time histories of the Fourier modal energies of (a) DNS1 and (b) DNS2.

$t = 53$, the flow is perturbed by adding Gaussian white noise of standard deviation 10^{-4} to the velocity components of all Fourier modes. We chose this particular time because it coincides with the maximum of kinetic energy in azimuthal wavenumber $m = 1$ and we expect the flow to have completed its initial spin-up by then. The perturbation level is sufficiently small to not affect the leading modes directly.

The rationale for considering both unperturbed and perturbed DNS should become evident below when we detail the comparison to experimentally obtained data. We note that up until $t = 53$, both DNS1 and DNS2 are nominally symmetric, i.e. $S = 0$, but that the random perturbation applied to DNS2 at this time breaks the symmetry. Symmetry is not expected to be precisely obtained in the experiment at any time owing to inevitable imperfections of the equipment, though the measure cannot be directly assessed from the available experimental data.

The experimental PIV data and the two DNS simulations were projected onto Kelvin modes using (3), and the time evolution of the corresponding amplitudes of the (1, 1, 1)-Kelvin mode, $a_1 = a_{1,1,1}$, are shown in Fig. 6. All three show the same initial evolution, with $a_{1,1,1}$ growing from zero (solid-body rotation) at $t = 0$ to a maximum value at about $t = 53$. Up to this point in time, the two DNS runs are identical, and at this time a perturbation is introduced in DNS2 (as described earlier). For the two DNS cases, their evolutions of a_1 track each other very closely until about $t = 150$. By $t \approx 200$, the temporal behaviour of a_1 for DNS2 becomes erratic, whereas for DNS1 the erratic temporal behaviour does not start until $t \approx 250$. Following the peak in a_1 at $t \approx 50$, the experimental a_1 remains at a higher level than that for either DNS case, and becomes erratic earlier, by about $t = 150$.

From the DNS, it is straightforward to examine temporal evolution of the Fourier modal energies E_m as shown in Fig. 7. For DNS1, modal energies evolve very much as if the forced $m = 1$ flow that is established by about $t = 100$ is unstable to a triadic resonance involving modes with $m = 4$ and 5 (as assessed from the leading exponential growth of energies in these two azimuthal wavenumbers which becomes evident near $t = 200$). It is only after the energies in these modes, E_4 and E_5, saturate at $t \approx 250$ that the flow starts to have erratic behaviour. In the DNS2 case, shortly after the perturbation is introduced, E_9 and higher Fourier modes grow exponentially. E_9 saturates at about $t = 150$ while E_4 and E_5 continue to grow exponentially and then saturate at $t \approx 200$, following which the flow becomes erratic.

Up to this point, we have considered global measures in order to analyse flow dynamics. Next we examine details of the instantaneous flow at strategically selected instants. Our measure for the experimental data is axial vorticity extracted on the single available measurement plane, while for the DNS data we show axial vorticity both on this plane and on its reflection about the cylinder equator in order to emphasise symmetry properties of the flow in addition to structure. We note that the times at which data are compared are not always precisely aligned between experiment and DNS. Our motivation is to emphasise broad similarities and differences between the various data sets.

At an early time, $t = 104$ as shown in Fig. 8(a, e, i), the structures evident in the experimental and numerical data are in good agreement and are dominated by shapes attributable to Fourier modes $m = 0$ and $m = 1$; the latter corresponding to the directly forced flow. We recall that at time $t = 53$, DNS2 was perturbed randomly, however, the vorticity contours on the two planes $z = \pm 0.25\Gamma$ apparently exhibit near-perfect $\mathcal{I}$-symmetry because the perturbation was small. This symmetry persists in the data for DNS1 at $t = 245$, but is broken at time $t = 735$ as may be deduced by a comparison of the upper and lower panels in Fig. 8(d). At $t = 245$, the structure corresponds principally to Fourier modes $m = 0$, 1, 4 and 5, as observed in Fig. 8(c), in agreement with the (global) Fourier modal energies shown at this time in Fig. 7(a).

One of the principal points motivating Fig. 8 may be seen from a comparison of experimental and numerical data shown in Fig. 8(f) and (j), where the presence of structure corresponding now to azimuthal Fourier modes $m = 9$ and 10 may be observed in both experiment and DNS2. These modes are never observed as dominant in the results for DNS1, and we may conclude that their presence in DNS2 is a consequence of the random perturbation delivered at $t = 53$. It may also be observed that the data at this time on the two planes $z = \pm 0.25\Gamma$ is not $\mathcal{I}$-symmetric, although

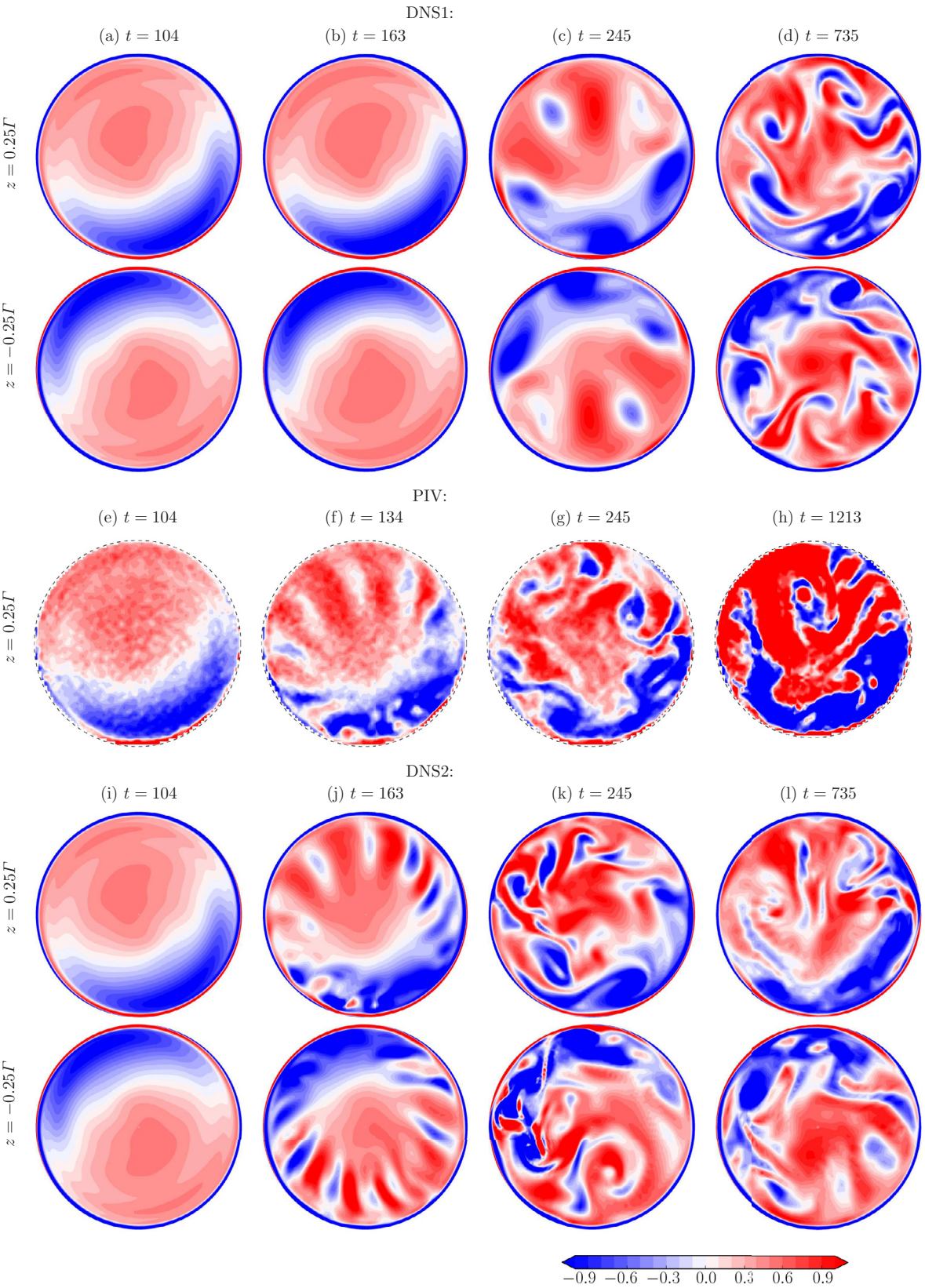

Fig. 8. Snap-shots of the non-dimensional axial vorticity from the two DNS cases and the experiment. For the experiment (e–h), data are only available on a single plane at elevation $z = 0.25\Gamma$. In considering DNS data, vorticity both on this plane and its equatorial reflection are shown in order to highlight symmetry properties of the flow. Colourmap levels are the same in all snapshots. Planes as viewed in the direction of vector $\boldsymbol{\Omega}_1$ in Fig. 1, with tilt direction indicated by the arrow (i.e., the vector drawn is the difference between $\boldsymbol{\Omega}_2$ and $\boldsymbol{\Omega}_1$ shown in Fig. 1).

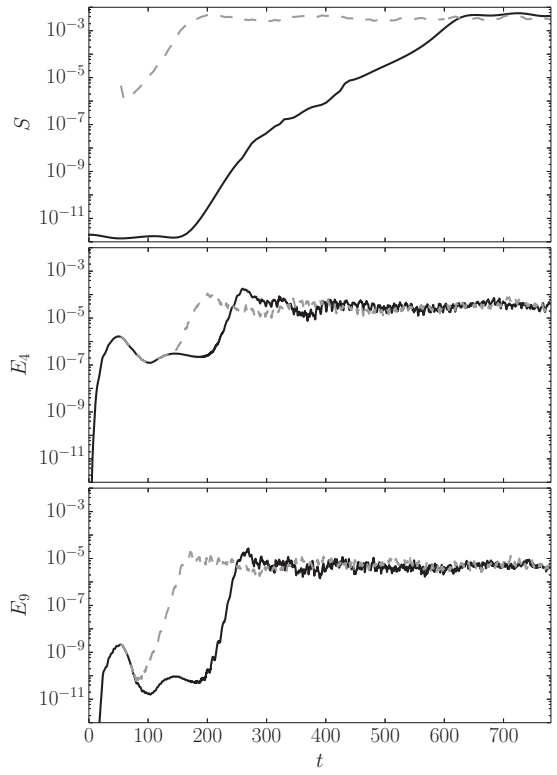

Fig. 9. Time series of the symmetry parameter S, and modal energies E_4 and E_9, for DNS1 (solid lines) and DNS2 (dashed lines).

there is a superficial similarity. At later times $t = 245$ and 735, the data for DNS2 have lost symmetry completely but exhibit structure comparable to that observed in the experiment at the later times.

The lack of inversion symmetry in the later-time snap-shots of DNS1 and DNS2 warrants closer inspection of the symmetry of the flows as they evolve. This is done by monitoring S during the evolution, and its time series is shown in the top panel of Fig. 9. In DNS1, where the initial condition is solid-body rotation at $\alpha = 0$ (which is $\mathcal{I}$-symmetric) and the cylinder is smoothly tilted to $\alpha = 15^\circ$, there are nominally no symmetry-breaking perturbations introduced (other than those due to numerical noise), S remains at numerical noise levels until about $t = 150$, which corresponds to the time when the triads associated with $m = 4$ and 5 are established, and then S starts to grow exponentially. This indicates that the $m = 1, 4, 5$ triad state is unstable to symmetry-breaking. The $m = 1, 4, 5$ triad state saturates before S saturates, and there is a transient period during which the triad state persists, but is progressively becoming more non-symmetric, and finally by $t \approx 600$, the symmetry is fully broken and DNS1 reaches its asymptotic state. In contrast, for DNS2, a substantial random perturbation was introduced at $t \approx 53$ which immediately broke the $\mathcal{I}$-symmetry, and S grows exponentially at the same rate as in DNS1, but from a level that is several orders of magnitude larger, and so it saturates much earlier (by $t \approx 200$). The other modal energies, and in particular E_9, also begin to grow much earlier in DNS2 due to the introduced perturbation, and result in a very different transient evolution compared to DNS1, but with several features in common with the transient evolution in the experiment. Finally, we note that the asymptotic states of both DNS1 and DNS2 are the same, as expected, which is confirmed by equal saturation levels of S, converged spectra of Fourier modal energy (not shown), and practically identical time-averaged flow which also matches the experiment, as shown in Fig 5.

6. Conclusions

We presented planar PIV measurements and DNS at matching parameters of a precessing cylinder flow at a tilt angle of 15°. These experiments are the first in a series aiming to conclusively explain the resonant collapse mechanism as observed by Johnson (1967), Malkus (1968) and Manasseh (1992). For a strongly-forced case which showed a rapid transition from a state dominated by the forced mode to a disordered state, structures of azimuthal wavenumber around $m \approx 9$ were observed. Amplitudes of projections onto Kelvin modes and Fourier analysis of the velocity field indicate that multiple azimuthal modes were present. Their wavenumbers are higher than those predicted by an unperturbed DNS, and they appear earlier.

However, a perturbation added to the DNS when the forced mode is maximum changes the leading modes to $m = 9$ and 10, promotes the transition process, and produces vortical structures during the transition which match corresponding PIV visualisations. This perturbation was shown to immediately break the symmetry of the flow, whereas the DNS without this perturbation was shown to also be unstable to symmetry breaking, but this manifested itself much later as the perturbation it was subjected to consisted of numerical noise. By comparing the DNS transients to the transients observed in the experiment, we conclude that the perturbations in the experiment are comparable, if not larger, than the perturbation introduced in DNS2, suggesting that analysis of time histories in such experiments need to take the noise levels into consideration.

Finally, moderately long periods in Fig. 7 where energy growth is clearly exponential warrant a comparison to weakly nonlinear theory (Lagrange et al., 2011), which has been successful for describing some of the phenomena observed in precessing cylinders (Albrecht et al., 2015). Hence, we have extracted growth rates from DNS and compared them to theory. For DNS1, we find $\sigma_4^{\mathrm{DNS}} = 0.1507$ for mode $m = 4$, and a larger $\sigma_9^{\mathrm{DNS}} = 0.1935$ for $m = 9$. Theoretical predictions are about 50% above the DNS values, $\sigma_4^{\mathrm{theory}} = 0.2356$ and $\sigma_9^{\mathrm{theory}} = 0.2684$, although the ratio of $\sigma_4^{\mathrm{theory}}/\sigma_9^{\mathrm{theory}} = 0.88$ is similar to its DNS counterpart of 0.78. In general however, this confirms the rather limited performance of weakly nonlinear theory in the present parameter regime well above the instability threshold, in accord with Albrecht et al. (2015).

Acknowledgements

We are grateful for financial support provided by Australian Research Council Discovery grant DP130101744, U. S. National Science Foundation grant CBET-1336410, and for resources provided by the Australian National Computational Infrastructure (NCI) via Merit Allocation Scheme Grant No. D77.

References

Albrecht, T., Blackburn, H.M., Lopez, J.M., Manasseh, R., Meunier, P., 2015. Triadic resonances in precessing rapidly rotating cylinder flows. J. Fluid Mech. 778, R1.
Blackburn, H.M., Albrecht, T., Mannaseh, R., Lopez, J.M., Meunier, P., 2014. Instability in a precessing cylinder flow. In: Proceedings of the 19th A/Asian Fluid Mechics Conference, Melbourne.
Blackburn, H.M., Sherwin, S.J., 2004. Formulation of a Galerkin spectral element—Fourier method for three-dimensional incompressible flows in cylindrical geometries. J. Comput. Phys. 197 (2), 759–778.
Giesecke, A., Albrecht, T., Gundrum, T., Herault, J., Stefani, F., 2015. Triadic resonances in nonlinear simulations of a fluid flow in a precessing cylinder. New J. Phys. 17 (11), 113044.
Johnson, L., 1967. The precessing cylinder. Notes on the 1967 Summer Study Program in Geophysical Fluid Dynamics at the Woods Hole Oceanographic Inst. Ref. 67–54.
Lagrange, R., Eloy, C., Nadal, F., Meunier, P., 2008. Instability of a fluid inside a precessing cylinder. Phys. Fluids 20, 081701.

Lagrange, R., Meunier, P., Nadal, F., Eloy, C., 2011. Precessional instability of a fluid cylinder. J. Fluid Mech. 666, 104–145.
Malkus, W.V.R., 1968. Precession of the Earth as the cause of geomegnetism. Science 160, 259–264.
Manasseh, R., 1992. Breakdown regimes of inertia waves in a precessing cylinder. J. Fluid Mech. 243, 261–296.
Manasseh, R., 1993. Visualizaton of the flows in precessing tanks with internal baffles. AIAA J. 31, 312–318.
Marques, F., Lopez, J.M., 2015. Precession of a rapidly rotating cylinder flow: traverse through the resonance. J. Fluid Mech. 782, 63–98.
Meunier, P., Eloy, C., Lagrange, R., Nadal, F., 2008. A rotating fluid cylinder subject to weak precession. J. Fluid Mech. 599, 405–440.